

## Universal Gate for Fixed-Frequency Qubits via a Tunable Bus

David C. McKay,<sup>1,\*</sup> Stefan Filipp,<sup>2</sup> Antonio Mezzacapo,<sup>1</sup> Easwar Magesan,<sup>1</sup>  
Jerry M. Chow,<sup>1</sup> and Jay M. Gambetta<sup>1</sup>

<sup>1</sup>IBM T.J. Watson Research Center, Yorktown Heights, New York 10598, USA

<sup>2</sup>IBM Research-Zurich, 8803 Rueschlikon, Switzerland

(Received 26 April 2016; revised manuscript received 18 August 2016; published 12 December 2016)

A challenge for constructing large circuits of superconducting qubits is to balance addressability, coherence, and coupling strength. High coherence can be attained by building circuits from fixed-frequency qubits; however, leading techniques cannot couple qubits that are far detuned. Here, we introduce a method based on a tunable bus which allows for the coupling of two fixed-frequency qubits even at large detunings. By parametrically oscillating the bus at the qubit-qubit detuning we enable a resonant exchange ( $XX + YY$ ) interaction. We use this interaction to implement a 183-ns two-qubit iSWAP gate between qubits separated in frequency by 854 MHz, with a measured average fidelity of 0.9823(4) from interleaved randomized benchmarking. This gate may be an enabling technology for surface-code circuits and for analog quantum simulation.

DOI: 10.1103/PhysRevApplied.6.064007

### I. INTRODUCTION

Superconducting qubits are a promising implementation for fault-tolerant quantum computing [1]; however, the proposed circuits will be large—a logical qubit in the surface code could require up to  $10^4$  physical qubits [2]. Building these large circuits requires highly coherent and strongly interacting physical qubits to achieve high-fidelity gates. At the same time, unwanted interactions which undermine the fault tolerance built into the surface code must be minimized. These divergent conditions on coherence, interaction, and cross talk have led to two main qubit architectures, depending on which condition is given highest priority.

In the first approach, the qubit frequencies are tunable and interactions are controlled by dynamically tuning pairs of qubits into and out of specific resonance conditions [3,4]. Although this tunability enables fast gates with relatively high on-to-off ratios, these qubits are susceptible to dephasing noise from the tunability channel—typically, flux noise—which lowers coherence [5]. Furthermore, this approach is sensitive to frequency crowding; as a pair of qubits tune into resonance, they must avoid crossing through resonances with other qubits. Utilizing longitudinal interactions (see, e.g., Refs. [6–11]) may alleviate these crowding issues, but interactions of this type have yet to be implemented.

The second approach is to use fixed-frequency qubits, which have demonstrated superior coherence properties in circuits implemented using two- [12] and three-dimensional [13,14] architectures. A number of gates have been proposed and realized for fixed-frequency qubits by applying one or more microwave drives [15–19]. For example, the cross-resonance gate [20,21]

has demonstrated fidelities greater than 0.99 [12]. However, similar to many drive-activated gates, it is only effective when the qubits are closely spaced compared to the anharmonicity (the detuning between the qubit transition and the transition to the next excited state). For the transmon qubit, used here and in a plurality of experiments, this constraint on cross resonance limits the frequency spacing to approximately a few hundred megahertz. For large circuits, this close spacing is challenging for fabrication, cross talk, and addressability.

Ideally, we would like to combine the best aspects from both approaches: the flexibility and scalability of tunable qubits with the coherence and fidelity of fixed-frequency qubits. This combination is possible when transferring tunability from the computational qubits to the coupling degree of freedom, thereby reducing sensitivity to noise. There are two implementations of a tunable coupler, direct and indirect. A direct tunable coupler is realized by a tunable circuit element between qubits, e.g., a flux-tunable inductor [22–26]. Alternatively, an indirect tunable coupling is realized by a fixed coupling to a tunable resonator. When the qubits are far detuned from the resonator—i.e., in the dispersive limit of the circuit-quantum-electrodynamics architecture—this arrangement realizes a tunable bus and the exchange coupling between the qubits can be tuned by changing the qubit-bus detuning [27–32]. Interactions can also be modulated by frequency-tuning constructive or destructive interference between different coupling paths [33]. Direct couplers are more compact, but qubits connected to the coupler are more sensitive to noise on the tuning degree of freedom; there is intrinsic protection from tuning noise for a tunable bus when we operate in the dispersive limit. Tunable couplers of both varieties have been realized in several experiments: between two tunable

\*dcmckay@us.ibm.com

qubits [24,29], between a qubit and a resonator [26,33], and between resonators [25,30,34].

In this work, we realize a tunable bus between high-coherence fixed-frequency qubits with a relative detuning much larger than the anharmonicity. To turn on the interaction between the qubits, we modulate the tunable bus at the qubit difference frequency (as theoretically proposed in several papers [22,27,35]) which causes a parametric oscillation of the qubit-qubit exchange coupling and activates a resonant  $XX + YY$  interaction [36,37]. The exchange interaction causes a two-qubit oscillation between states with one excitation  $|10\rangle$  and  $|01\rangle$ —i.e., qubit 1 ( $Q1$ ) in the excited state, qubit 2 ( $Q2$ ) in the ground state, and vice versa. Applying this interaction for 183 ns, we demonstrate a universal two-qubit gate—the *iswap* gate—with a 0.982 average gate fidelity. Unlike drive-activated gates, the exchange-interaction strength does not decrease when the qubit-qubit detuning is larger than the anharmonicity. For example, for the detunings of the device in this work, 854 MHz, the leading gate for fixed-frequency qubits, cross-resonance [12], would not be viable. Although we demonstrate the gate between a single pair of qubits, multiple qubits can, in general, be coupled to a single bus since the interaction is resonant in the detuning between specific qubit pairs. Therefore, the *iswap* gate is promising for implementing larger circuits where a range of qubit frequencies is needed to avoid cross talk and addressing errors. In addition, the tunable-bus architecture enables analog quantum-simulation schemes requiring controllable interactions. Specifically, with this type of coupling,  $ZZ$  and  $XX-YY$  two-photon interactions can also be activated by adjusting the modulation frequency. Moreover, the tunable bus can be used to more efficiently realize surface-code implementations requiring *iswap* gates [38].

Our paper is organized as follows. In Sec. II A, we discuss the theory of the tunable-bus device and, in Sec. II B, we introduce our two-qubit device. In Sec. III, we show two-qubit *iswap* oscillations using our device and prepare and characterize a Bell state. In Sec. IV, we present our universal two-qubit *iswap* gate and characterize the gate using randomized benchmarking and quantum-process tomography. We conclude with a discussion in Sec. V.

## II. TUNABLE BUS

### A. Theory

The tunable-bus circuit that we consider in this paper consists of several fixed-frequency qubits dispersively coupled to a frequency-tunable bus; a circuit schematic is shown in Fig. 1(a). Because the bus is in the ground state and dispersively coupled, it suffices to keep only the first two levels of the bus. In terms of  $N$  bare qubits coupled to a tunable bus, the standard circuit-QED Hamiltonian is

$$\frac{H}{\hbar} = \sum_{i=1}^N \left[ -\frac{\omega_i \hat{\sigma}_i^Z}{2} + g_i (\hat{\sigma}_i^+ \hat{\sigma}_{\text{TB}}^- + \hat{\sigma}_i^- \hat{\sigma}_{\text{TB}}^+) \right] - \frac{\omega_{\text{TB}}(\Phi) \hat{\sigma}_{\text{TB}}^Z}{2}, \quad (1)$$

where  $\hat{\sigma}^Z$  is the Pauli-Z operator and  $\hat{\sigma}^+$  ( $\hat{\sigma}^-$ ) is the raising (lowering) operator. The tunable bus (TB) tunes with flux  $\Phi$  as [5]

$$\omega_{\text{TB}}(\Phi) = \omega_{\text{TB},0} \sqrt{|\cos(\pi\Phi/\Phi_0)|}, \quad (2)$$

where  $\Phi_0$  is the flux quantum. In the dispersive regime, i.e.,  $|g_i/(\omega_i - \omega_{\text{TB}})| \ll 1$ , we can adiabatically eliminate the TB,

$$\frac{H}{\hbar} = \sum_i^N -\frac{\tilde{\omega}_i(\Phi) \hat{\sigma}_i^Z}{2} + \sum_{j>i}^N J_{ij}(\Phi) (\hat{\sigma}_i^+ \hat{\sigma}_j^- + \hat{\sigma}_i^- \hat{\sigma}_j^+), \quad (3)$$

thus realizing a flux-tunable coupler. In Eq. (3),  $\tilde{\omega}$  is the dressed qubit energy and  $J_{ij}$  is the exchange coupling between qubits  $i$  and  $j$ , which depend on the flux as

$$\tilde{\omega}_i = \omega_i + \frac{g_i^2}{\Delta_i(\Phi)}, \quad (4)$$

$$J_{ij} = \frac{g_i g_j}{2} \left( \frac{1}{\Delta_i(\Phi)} + \frac{1}{\Delta_j(\Phi)} \right), \quad (5)$$

where  $\Delta_i(\Phi) = \omega_i - \omega_{\text{TB}}(\Phi)$ . To interact the qubits via the tunable coupler, we apply a sinusoidal fast-flux-bias modulation of amplitude  $\delta$  so that the total flux applied to the tunable bus is  $\Phi(t) = \Theta + \delta \cos(\omega_\Phi t)$ . Expanding  $\tilde{\omega}_i$  in the parameter  $\delta \cos(\omega_\Phi t)$  to second order where  $\delta \ll 1$ , we obtain

$$\begin{aligned} \tilde{\omega}_i[\Phi(t)] &\approx \tilde{\omega}_{\Phi_i}(\Theta) + \left. \frac{\partial \tilde{\omega}_i}{\partial \Phi} \right|_{\Phi \rightarrow \Theta} \delta \cos(\omega_\Phi t) \\ &+ \frac{1}{2} \left. \frac{\partial^2 \tilde{\omega}_i}{\partial \Phi^2} \right|_{\Phi \rightarrow \Theta} [\delta \cos(\omega_\Phi t)]^2, \quad (6) \\ &= \left[ \tilde{\omega}_i(\Theta) - \frac{\delta^2}{4} \left. \frac{\partial^2 \tilde{\omega}_i}{\partial \Phi^2} \right|_{\Phi \rightarrow \Theta} \right] \\ &+ \left. \frac{\partial \tilde{\omega}_i}{\partial \Phi} \right|_{\Phi \rightarrow \Theta} \delta \cos(\omega_\Phi t) \\ &+ \frac{\delta^2}{4} \left. \frac{\partial^2 \tilde{\omega}_i}{\partial \Phi^2} \right|_{\Phi \rightarrow \Theta} \cos(2\omega_\Phi t). \quad (7) \end{aligned}$$

Since the relation between qubit frequency and flux is nonlinear, there is a second-order dc shift and an oscillating term at  $2\omega_\Phi$ ; a similar expansion holds for  $J_{ij}$ . Typical values for these expansion terms are shown in Fig. 1(b). In the frame rotating at the qubit frequencies for  $\delta = 0$  (the measurement frame), oscillating  $\hat{\sigma}_Z$  terms and dc exchange-coupling terms time average to zero. Therefore,

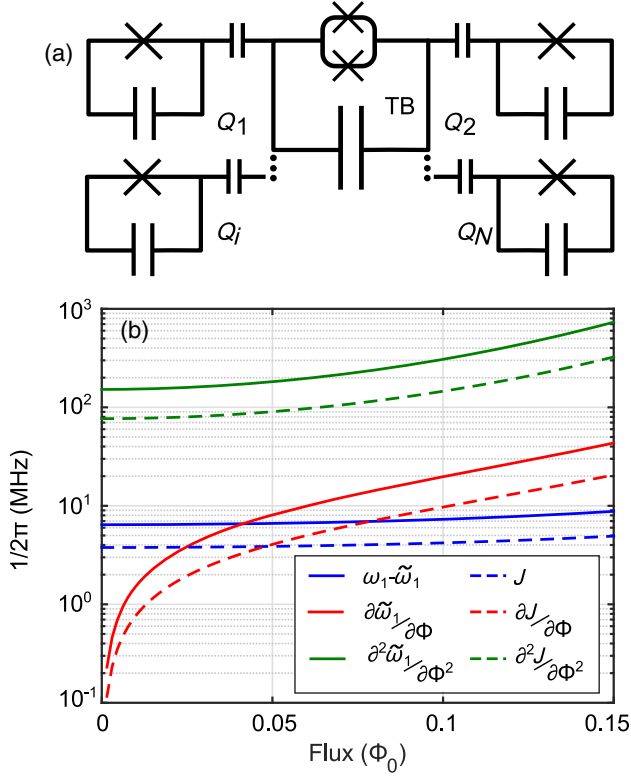


FIG. 1. (a) Schematic of an  $N$  qubit, one-bus device. (b) Size of the expansion terms for  $\omega$  and  $J$  versus the dc flux tuning the bus. Calculations are for the device parameters given in Sec. II B.

updating Eq. (3) to include all other expansion terms, the Hamiltonian becomes

$$\begin{aligned} \frac{H}{\hbar} = & \sum_i^N - \left( \tilde{\omega}_i - \frac{\delta^2}{4} \frac{\partial^2 \tilde{\omega}_i}{\partial \Phi^2} \right) \frac{\hat{\sigma}_i^Z}{2} \\ & + \sum_{j>i}^N \left[ \delta \frac{\partial J_{ij}}{\partial \Phi} \cos(\omega_\Phi t) - \frac{\delta^2}{4} \frac{\partial^2 J_{ij}}{\partial \Phi^2} \cos(2\omega_\Phi t) \right] \\ & \times (\hat{\sigma}_i^+ \hat{\sigma}_j^- + \hat{\sigma}_i^- \hat{\sigma}_j^+), \end{aligned} \quad (8)$$

where all values are evaluated at  $\Phi = \Theta$ . Because there is a drive-induced qubit shift, all  $N$  qubits will acquire a phase during the flux-modulation pulse. This phase may be compensated for by applying single-qubit  $Z$  gates. In a frame rotating at the qubit frequencies (including the drive-induced shift), the Hamiltonian is

$$\begin{aligned} \frac{H}{\hbar} = & \sum_{i,j>i}^N \left[ \delta \frac{\partial J_{ij}}{\partial \Phi} \cos(\omega_\Phi t) + \frac{\delta^2}{4} \frac{\partial^2 J_{ij}}{\partial \Phi^2} \cos(2\omega_\Phi t) \right] \\ & \times e^{i\Delta_{ij,\delta} t} (\hat{\sigma}_i^+ \hat{\sigma}_j^- + \hat{\sigma}_i^- \hat{\sigma}_j^+), \end{aligned} \quad (9)$$

where  $\Delta_{ij,\delta} = (\tilde{\omega}_i - \tilde{\omega}_j) + (\delta^2/4)[(\partial^2 \tilde{\omega}_j / \partial \Phi^2) - (\partial^2 \tilde{\omega}_i / \partial \Phi^2)]$ . When  $\omega_\Phi$  is resonant with  $\Delta_{ij,\delta}$ , the Hamiltonian is

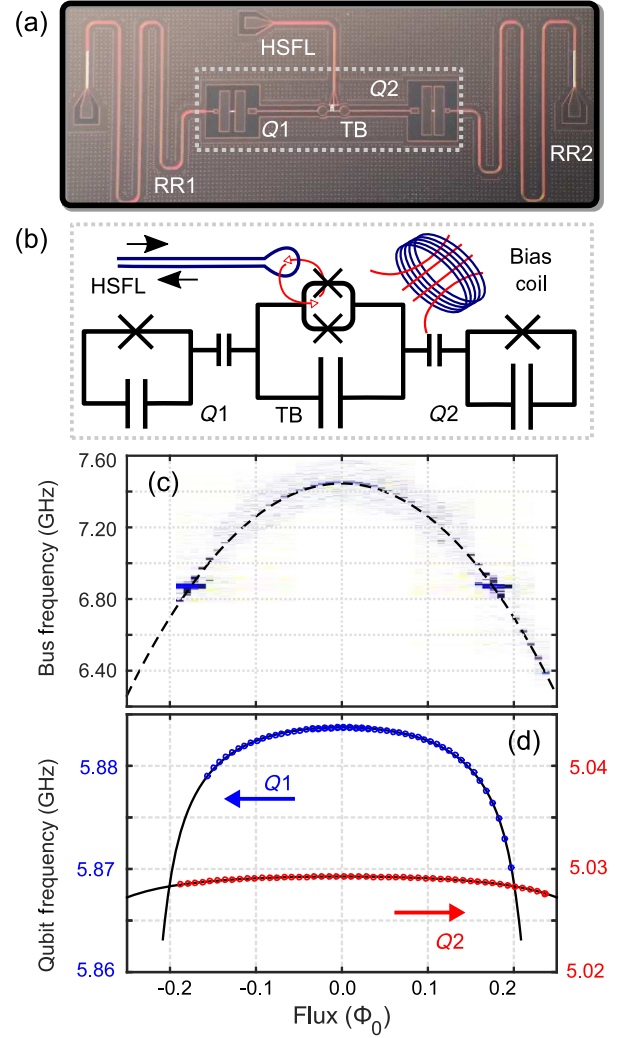


FIG. 2. (a) Optical image and (b) schematic of our circuit consisting of two fixed-frequency transmon qubits ( $Q1$ ,  $Q2$ ) coupled via a third tunable bus qubit (“tunable bus,” TB).  $Q1$  and  $Q2$  have individual readout resonators (RR1, RR2). The TB is tuned by a dc-bias coil and a high-speed flux line (HSFL). Spectroscopy of (c) TB and (d)  $Q1$ ,  $Q2$  frequency versus dc flux;  $Q1$  tunes more strongly with flux because it is closer in frequency to the TB. We fit these tuning curves (the solid lines) using Eq. (4) to extract the Hamiltonian parameters for Eq. (1).

$$\frac{H}{\hbar} = \frac{\delta}{2} \frac{\partial J_{ij}}{\partial \Phi} (\hat{\sigma}_i^X \hat{\sigma}_j^X + \hat{\sigma}_i^Y \hat{\sigma}_j^Y), \quad (10)$$

which is a resonant exchange interaction between qubits  $i$  and  $j$  only. There can also be a resonance condition when  $2\omega_\Phi = \Delta_{ij,\delta}$  with a different exchange coefficient. The interaction described by Eq. (10) couples any states in the same excitation manifold. For two qubits, this coupling involves only the set of states  $\{|10\rangle, |01\rangle\}$ . Applying this interaction for certain periods of time can generate entanglement and be used as a two-qubit gate. This effect will be explored in Secs. III and IV.

## B. Experimental device

Our experimental implementation of a two-qubit, one-bus device is shown in Fig. 2. By varying the dc flux, we can use Eqs. (2) and (4) to extract the bare Hamiltonian parameters  $g_1(g_2)/2\pi = 100.0(71.4)$  MHz,  $\omega_1(\omega_2)/2\pi = 5.8899(5.0311)$  GHz,  $\omega_{\text{TB},0}/2\pi = 7.445$  GHz by fitting to the measured frequencies  $\omega_{\text{TB}}$ ,  $\tilde{\omega}_1$ , and  $\tilde{\omega}_2$  as shown in Fig. 2. These transmon qubits have anharmonicity  $\alpha/2\pi = -324(235)$  MHz, where  $\alpha$  is the detuning between the  $|1\rangle \rightarrow |2\rangle$  transition and the qubit transition  $|0\rangle \rightarrow |1\rangle$ . One trade-off of the tunable-bus design is that the dressed qubits are susceptible to flux noise since the frequencies are flux tunable. However, compared to a directly tunable qubit, the flux noise sensitivity is lowered by a factor of  $(g/\Delta)^2$ . This noise has a minimal effect on our 23-ns single-qubit gates. At the flux-bias point used to implement the two-qubit gate,  $T_1 = 26.3(7)[50(3)] \mu\text{s}$  and  $T_2 = 12.1(4)[28(1)] \mu\text{s}$  for  $Q1$  ( $Q2$ ) and the single-qubit fidelity measured from randomized benchmarking is 0.99909(2) [0.99949(1)] (see the Supplemental Material [39] for benchmarking data and coherence measurements).

## III. TWO-QUBIT $i\text{SWAP}$ OSCILLATIONS

To experimentally measure the exchange interaction, we perform a  $\pi$  pulse to prepare the state  $|10\rangle$  (or  $|01\rangle$ ) and then apply sinusoidal flux-modulation pulses of strength  $\delta$  and drive frequency  $\omega_\phi$  in a range around 854 MHz to couple the states and drive exchange oscillations. The flux-pulse shape is shown in Fig. 3(a) and sample oscillations are illustrated in Fig. 3(b). In order to effectively drive these oscillations, the tunable bus must be dc flux biased ( $\Theta = -0.108\Phi_0$ ) since the strength of the exchange rate is proportional to the slope of the bus tuning curve, Eq. (10). The slope is not purely linear, so we also get a sizable dc shift of the bus frequency, which in turn shifts the qubit frequency as given by Eq. (8). We can measure the qubit shift during the oscillation by performing a Ramsey interferometric experiment: starting in the state  $|00\rangle$ , we apply a  $\pi/2$  pulse to the qubit, then exchange for time  $t$  (at a given flux-modulation amplitude), reverse the exchange for time  $t$  (flip the flux-modulation pulse phase by  $180^\circ$ ) to return to the original state, then apply a final  $\pi/2$  to the qubit. The fringe frequency measures the induced shift on the qubit frequency. The qubit shift versus the exchange rate is plotted in Fig. 3(c). Using the bare-qubit parameters, we construct a no-free-parameter-theory curve (the solid line).

These qubit shifts have two important consequences for constructing a gate. For one, they are equivalent to applying single-qubit  $Z$  gates, which, therefore, need to be compensated for. Second, as we increase the exchange rate, the coupler moves into closer resonance with the qubit. As discussed above, this change in detuning reduces the protection to flux noise [i.e.,  $(g/\Delta)^2$  increases]. Additionally, increasing the drive strength can lead to leakage out of the computational basis into the higher

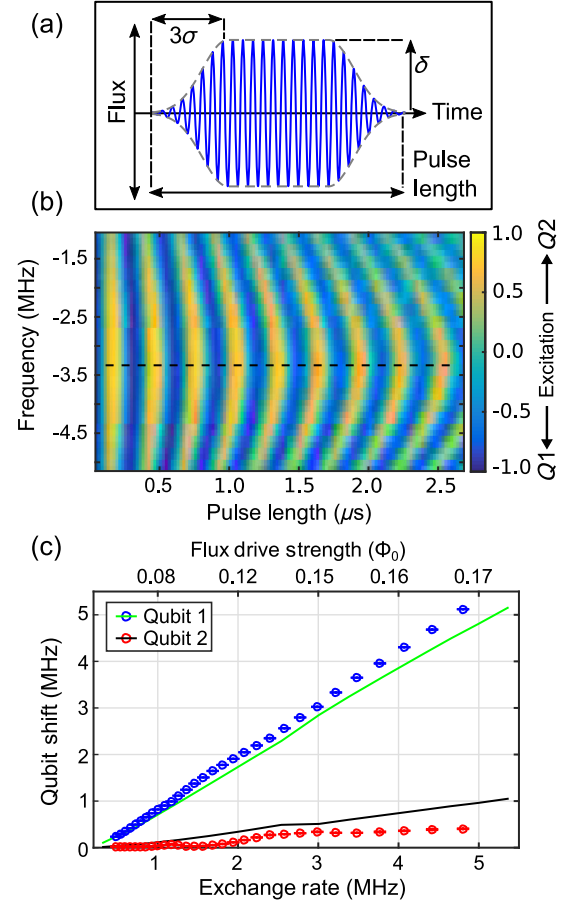


FIG. 3. (a) Flux-modulation pulse of strength  $\delta$ . The pulse envelope (the gray dashed line) is a square pulse with Gaussian turn on and off with  $\sigma = 8.3$  ns and the turn on or off time is  $3\sigma$ . (b) Exchange oscillations between  $|10\rangle$  and  $|01\rangle$  as a function of the flux-pulse length and the drive frequency  $\omega_\phi$  (with respect to the detuning between the qubits when  $\delta = 0$ ,  $\Delta_{12,\delta=0} \approx 854$  MHz). These data are taken at a dc flux bias of  $\Theta = -0.108\Phi_0$  with a constant flux-pulse height  $\delta = 0.153\Phi_0$ . The flux modulation induces a dc shift of the tunable bus, so the resonance frequency (the dotted line) of the exchange oscillation is shifted down from  $\Delta_{12,\delta=0}$  by approximately 3 MHz. (c) Qubit shifts during the flux-modulation pulse as a function of the drive strength (the procedure is described in the main text). The drive strength is plotted in terms of the measured exchange rate (the bottom axis) and the flux-modulation strength  $\delta$  in units of  $\Phi_0$  (the top axis) calculated theoretically from this exchange rate. The solid lines are no-free-parameter numerical calculations of the exchange rate and shift given a certain flux modulation by solving Eq. (1).

transmon levels and/or into the bus. Consequently, there is a trade-off between coherence, leakage, and exchange rate which puts an effective upper bound on how fast we can operate a two-qubit gate.

### A. $\sqrt{i\text{SWAP}}$ Bell state

Specific flux-modulation pulse lengths in Fig. 3 represent primitive two-qubit gates that can be used to

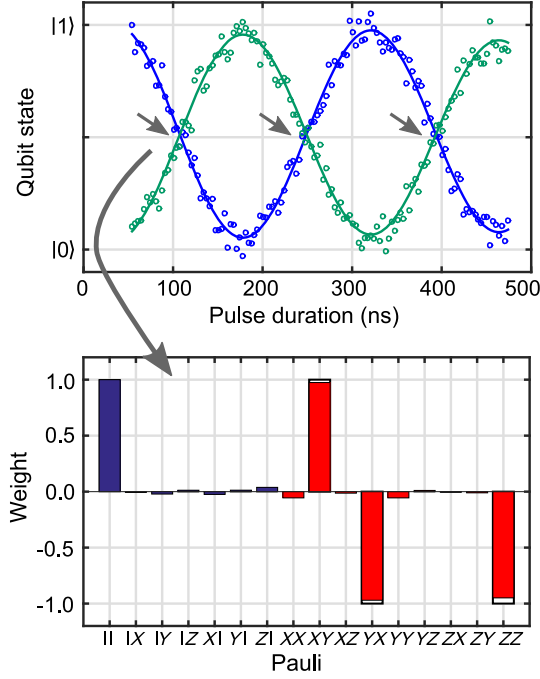


FIG. 4. (a) On-resonance SWAP oscillations between the qubits. We first apply a  $\pi$  pulse to  $Q1$ , then perform a variable-length flux-modulation pulse on the tunable bus with  $\omega_\phi/2\pi = 850.6$  MHz and  $\delta = 0.155\Phi_0$ . The excitation oscillates between the two qubits and, at special evolution times (indicated by arrows), entangled states are generated. (b) State tomography of the first entangled state in the Pauli representation, with a fidelity of 0.974. Single-qubit terms are illustrated in blue and two-qubit terms in red. The outlined bars show the ideal state,  $|\Psi\rangle = (|10\rangle - i|01\rangle)/\sqrt{2}$ .

construct a universal gate set for quantum computing. As indicated by the arrows in Fig. 4(a), there are certain locations,  $\Omega t = \pi(1/4 + n/2)$  (with  $\Omega$  being the exchange rate), where the excitation is equally shared between both qubits. At these points, a maximally entangled Bell state can be generated. At the first such crossing, it is possible to realize a  $\sqrt{i}$ SWAP gate, or  $i$ SWAP  $\pi/2$ . Applying a  $\sqrt{i}$ SWAP gate to either the state  $|10\rangle$  or  $|01\rangle$  generates a maximally entangled Bell state. We perform state tomography on such a state and measure a fidelity of 0.974, as illustrated in Fig. 4(b).

#### IV. $i$ SWAP GATE

The  $\sqrt{i}$ SWAP gate is not in the Clifford group and so is not suitable for randomized benchmarking or as an error correction primitive. By extending the modulation pulse so that  $\Omega t = \pi/2$ , we realize the  $i$ SWAP gate ( $i$ SWAP  $\pi$ ), which is in the Clifford group. This gate swaps the states  $|10\rangle, |01\rangle$  with a  $90^\circ$  phase with respect to the  $|00\rangle, |11\rangle$  states which are unchanged (see the inset of Fig. 6). The fidelity of this gate is sensitive to parasitic ZZ-type interactions (e.g., a controlled phase). However, because the detuning between our qubits is large, the ZZ interaction is only 66 kHz.

#### A. Gate optimization and simulation

To first optimize the  $i$ SWAP gate, we compare the gate error from two-qubit randomized benchmarking (RB) (see Sec. IV B) and simulation versus the gate length for  $\Theta = -0.108\Phi_0$ . For the numerics, we model the system as Duffing oscillators (truncated to three levels in the calculation), as given by the Hamiltonian

$$H_N = \sum_{i=1}^2 \left[ \omega_i a_i^\dagger a_i - \frac{\alpha_i}{2} (1 - a_i^\dagger a_i) a_i^\dagger a_i \right] + \omega_{\text{TB}} [\Phi(t)] a_{\text{TB}}^\dagger a_{\text{TB}} - \frac{\alpha_{\text{TB}}}{2} (1 - a_{\text{TB}}^\dagger a_{\text{TB}}) a_{\text{TB}}^\dagger a_{\text{TB}} + \sum_{i=1}^2 g_i (a_i^\dagger + a_i) (a_{\text{TB}}^\dagger + a_{\text{TB}}), \quad (11)$$

which is the transmon generalization of Eq. (1). Here, we define creation (annihilation) operators for the  $i$ th fixed frequency qubit  $a_i^\dagger$  ( $a_i$ ), with (0–1)-level transition energies  $\omega_i$  and anharmonicities  $\alpha_i$ . Similar definitions are given for the tunable bus, with operators  $a_{\text{TB}}^\dagger$  ( $a_{\text{TB}}$ ), and the time-dependent frequency  $\omega_{\text{TB}}[\Phi(t)]$ . The bus frequency as a function of flux is given by Eq. (2) and the time-dependent flux pulse is the same shape as in the experiment, as shown in Fig. 3(a). For the calculation, we work in the measurement basis obtained by numerically diagonalizing Eq. (11) when  $\omega_{\text{TB}}[\Phi(t)] = \omega_{\text{TB}}(\Theta)$ . The unitary transformation to the measurement basis from  $H_{N,0}$  is given by  $U_{N,0}$ . In a rotating frame at the dressed qubit frequencies, the dynamics of the time-dependent flux pulse are described by the interaction Hamiltonian,

$$H_I(t) = U_I \{ \omega_{\text{TB}}[\Phi(t)] - \omega_{\text{TB}}(\Theta) \} a_{\text{TB}}^\dagger a_{\text{TB}} U_I^\dagger, \quad (12)$$

$$U_I = e^{-i(U_{N,0}^\dagger H_{N,0} U_{N,0})t} U_{N,0}. \quad (13)$$

For both the experiment and the simulation, we calibrate  $\delta$  and  $\omega_\phi$  for a fixed pulse length. Experimentally,  $\omega_\phi$  is calibrated by optimizing the oscillation contrast and  $\delta$  by minimizing the error in the two-qubit rotation angle via error-amplification techniques. The simulation parameters are calibrated numerically by evolving the state  $|01\rangle$  by  $H_I$  for a fixed gate time to state  $|\Psi\rangle$  and optimizing the overlap  $|\langle\Psi|10\rangle|^2$  (1 for a perfect  $i$ SWAP gate), as a function of the drive amplitude  $\delta$  and the drive frequency  $\omega_\phi$ . The additional phases on the qubits in the measurement frame are also numerically and experimentally calibrated.

Using these procedures, we calibrate the gate experimentally and numerically for different gate times. Decoherence effects are included numerically by solving a master equation for the density matrix of the system

$$\dot{\rho} = -i[H_I, \rho] + \sum_{i=1}^2 \left[ \Gamma_{-,i}^{\text{dc}} \mathcal{D}[\sigma_i^-] \rho + \frac{\Gamma_{\phi,i}^{\text{dc}}}{2} \mathcal{D}[\sigma_i^Z] \rho \right]. \quad (14)$$

The superoperator  $D[\hat{O}]\rho$  is defined in the standard way,  $D[\hat{O}]\rho = (2\hat{O}\rho\hat{O}^\dagger - \hat{O}^\dagger\hat{O}\rho - \rho\hat{O}^\dagger\hat{O})/2$ . The effective damping and  $Z$  operators  $\sigma_i^-$ ,  $\sigma_i^Z$  are defined in the measurement basis for the first two levels of the transmon qubits. For each gate time, we compute the average gate fidelity,

$$F = \int d\Psi \langle \Psi | U_{\text{iSWAP}}^\dagger \rho_{|\Psi\rangle} U_{\text{iSWAP}} | \Psi \rangle, \quad (15)$$

where  $\rho_{|\Psi\rangle}$  is the resulting density matrix after evolving Eq. (14) with input state  $|\Psi\rangle$ , and  $U_{\text{iSWAP}}$  is the ideal iSWAP gate. There may be additional sources of error in the actual experiment such as  $1/f$  flux noise and coupler losses, which are not considered in this calculation. Both the experimental and theoretical results for the gate error  $1 - F$  are shown in Fig. 5(a). Numerically, we observe an optimal gate time of around 150 ns. For shorter gate times, the error rate increases substantially (likely due to leakage, which will be discussed next), while, for longer times, decoherence imposes a lower bound on the gate error. Note that there are two sets of experimental measurements of the gate error; one set is obtained by measuring the ground state of qubit 1 (tracing over qubit 2) and the other by measuring the ground state of qubit 2. It should be emphasized that these measurements are from the same experiment, i.e., we perform a set of two-qubit Clifford gates using the iSWAP gate as a primitive and then measure the average state of both qubit 1 and qubit 2 simultaneously through independent readouts. RB theory predicts that these measurements should give the same value for the fidelity since the random Clifford sequences mix errors equally to both qubits. However, we see a slight discrepancy between these two measurements that increases as we go to shorter gate times; e.g., at a gate length of 155 ns, the error per gate differs by  $4.4 \times 10^{-3}$ . The source of said discrepancy is an ongoing investigation. Nevertheless, both measures of fidelity show the same trend and are consistent with the numerical data. The optimal fidelity for the experimental data suggests a slightly longer gate of approximately 180 ns and, for further gate characterization (Sec. IV B), we select a gate time of 183 ns.

Increased error for short times is likely due to leakage out of the computational subspace. There are primarily two paths for leakage with this type of gate. The first path is a direct sideband drive from  $Q1$  or  $Q2$  to the tunable bus. This process is first-order but is strongly off resonance by ensuring that  $|\Delta_{i,\text{TB}}| \gg |\Delta_{12}|$ . The second path is from  $|11\rangle \rightarrow |20\rangle, |20\rangle$  because our physical qubits are transmons, and the resonant exchange interaction can also couple the set of states  $\{|11\rangle, |20\rangle, |02\rangle\}$ . The detuning of this transition compared to the wanted SWAP transition is

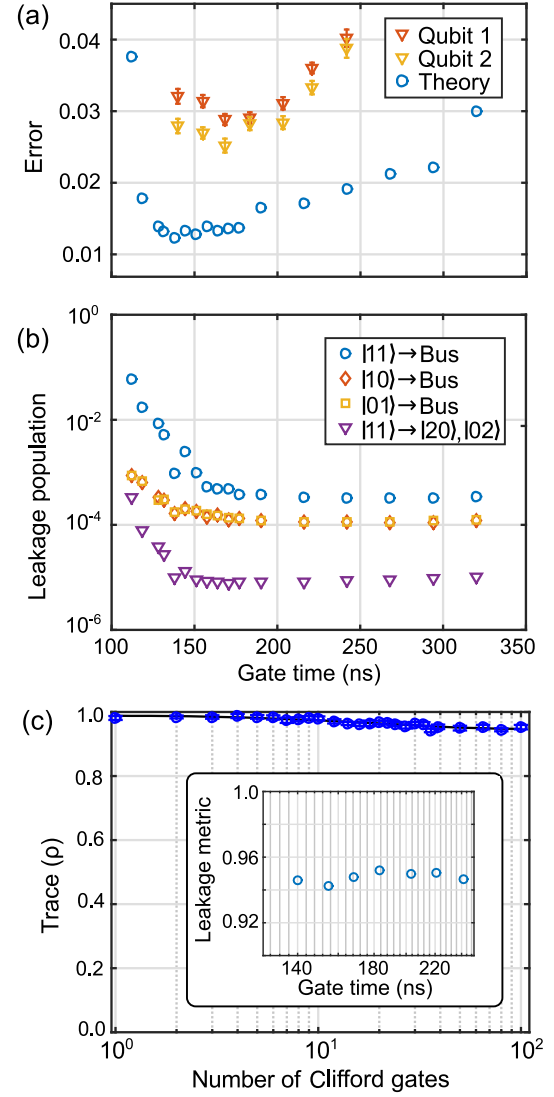


FIG. 5. Optimization and simulation of the iSWAP gate. (a) Gate error versus pulse width measured experimentally (the triangles) versus the numerical calculation (the circles), including levels outside the computational basis and decoherence. (b) Calculated leakage versus pulse width for different levels outside the computational basis. (c) Leakage measured experimentally by proxy by tracing over the computational states (leakage RB). These data are for the standard gate length 183 ns. (Inset) The leakage metric (the asymptote of the RB data) versus the pulse width. Because the leakage metric is flat versus the pulse width, we are not in the high-leakage regime seen in the numerics (b).

$$|2\omega_{1/2} + \alpha_{1/2} - (\omega_1 + \omega_2)| - |\Delta_{12}|, \quad (16)$$

$$|\Delta_{12/21} + \alpha_{1/2}| - |\Delta_{12}|. \quad (17)$$

For a large detuning compared to the anharmonicity, this transition is off resonant by the anharmonicity, which is large compared to the swap rate. For example, in our sample,  $|\Delta_{12}|/2\pi = 854$  MHz,  $|\Delta_{12} + \alpha_1|/2\pi = 530$  MHz, and  $|\Delta_{21} + \alpha_2|/2\pi = 1089$  MHz. From the numerics, we

can directly estimate leakage by evolving according to  $H_I$ , starting in the four basis states  $|00\rangle$ ,  $|01\rangle$ ,  $|10\rangle$ ,  $|11\rangle$  and calculating the population in higher excited states after the gate. At short gate times, leakage is a considerable issue, but it becomes negligible as the gate time increases past approximately 140 ns. The simulation results are shown in Fig. 5(b).

To characterize leakage experimentally, we perform a variation of the RB process. First, we perform standard two-qubit RB and measure the average state of both qubits. The value measured on qubit 1 (normalized so that  $|0\rangle$  is 1 and  $|1\rangle$  is 0) is  $\rho_{00} + \rho_{01} + \xi_1$ , where  $\xi_1$  represents leakage. Next, we repeat the same experiment with a  $\pi$  pulse at the end so that the measured state is now  $\rho_{10} + \rho_{11} + \xi_1$ , where  $\rho$  is the density matrix just before the  $\pi$  pulse and  $\xi$  is unchanged by the pulse. Adding the qubits and measurements together, we get

$$\begin{aligned} & (\rho_{00} + \rho_{01} + \xi_1) + (\rho_{00} + \rho_{10} + \xi_2) \\ & + (\rho_{10} + \rho_{11} + \xi_1) + (\rho_{01} + \rho_{11} + \xi_2) \\ & = 2[\text{Tr}(\rho) + \xi_1 + \xi_2]. \end{aligned} \quad (18)$$

The exact values of  $\xi_1$ ,  $\xi_2$  are unknown because they depend on the leakage states; however, under the assumption that they cause a deviation in the measurement signal, we can look at this measure as a function of the RB sequence length to observe leakage trends. In Fig. 5(c), we illustrate a representative leakage measurement for a 183-ns gate. Typical data asymptote from one, and we can define the asymptotic value to represent a leakage metric. Plotting the leakage metric versus the gate length [the inset of Fig. 5(c)], we see that there is no strong evidence of increasing leakage as we decrease the gate length. We conclude that we are not in the strong-leakage regime predicted by numerics and that leakage is not our limiting error.

### B. Gate characterization

Finally, we perform full characterization of our optimal gate-length iSWAP of 183 ns with both RB [40] and quantum-process tomography. When composing two-qubit Clifford gates for RB from this gate set, there are, on average, 1.5 iSWAP gates per Clifford. The ground-state population of  $Q_2$  as a function of the number of Clifford gates is shown in Fig. 6(a). If we assume that the error per Clifford gate is predominantly due to the iSWAP gate; i.e., the single-qubit gates are effectively perfect, the error per gate averaged over eight independent RB runs of 20 random seeds is  $2.77(1) \times 10^{-2}$ . A more-direct error measurement is obtained by interleaved RB [41], as is also shown in Fig. 6(a). Comparing the decay of the interleaved curve to the standard RB curve, we extract an error of  $1.77(4) \times 10^{-2}$  (with systematic error bounds of  $[0, 0.08]$ ). The measured error differs by approximately

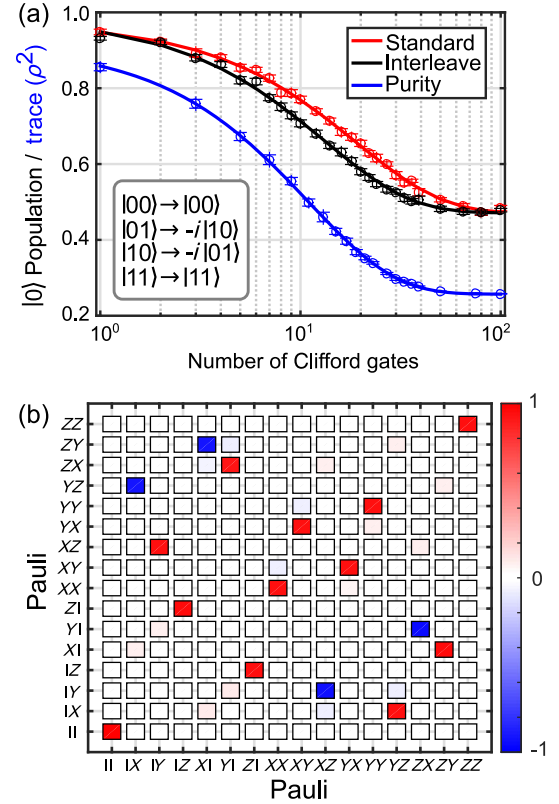


FIG. 6. (a) Standard, interleaved, and purity randomized benchmarking (RB) of the two-qubit iSWAP gate, with the state transformation shown in the inset. For standard and interleaved RB, the ground-state population of qubit 2 is plotted as a function of the number of Clifford gates for a sample RB run consisting of 20 random seeds (14 seeds for the purity RB). The error numbers quoted in the main text are averaged over eight such independent runs. For purity RB, we plot the trace of  $\rho^2$  versus the number of Clifford gates. (b) Pauli transfer matrix of the iSWAP gate measured from quantum-process tomography.

$2 \times 10^{-3}$  whether we fit to the average ground-state population of  $Q_1$  or  $Q_2$  (these quantities are measured in the same experiment). Here, we have quoted the more conservative of the two values. We also perform full quantum-process tomography (QPT) on the gate, as shown in Fig. 6(b). For this measurement, we use 8000 measurements with a readout fidelity of 0.70 (0.73) for  $Q_1$  ( $Q_2$ ). The fidelity from QPT is 0.949 from maximum-likelihood estimation and 0.96 from the raw linear inversion. While QPT gives a full description of the gate in terms of the Pauli transfer matrix, it is susceptible to state preparation and measurement errors.

The estimated gate error from simulation is  $1.5 \times 10^{-2}$ , which is slightly lower than the measured error. To confirm that the discrepancy between the measured and calculated error rates is not due to coherent gate errors, e.g., calibration, we perform purity RB [42], as shown in Fig. 6(a). For purity RB, we measure the trace of  $\rho^2$  ( $\rho$  is measured from state tomography) after the RB sequence;

these sequences are the same as the ones used for the standard RB measurement. Assuming a pure depolarizing noise  $\gamma$ , the density matrix after  $n$  Clifford gates (starting in the ground-state density matrix  $\rho_0$ ) is

$$\rho(n) = \gamma^n \rho_0 + (1 - \gamma^n) \frac{\mathcal{I}}{d}, \quad (19)$$

$$\begin{aligned} \rho^2(n) &= \gamma^{2n} \rho_0^2 + (1 - \gamma^n)^2 \frac{\mathcal{I}}{d^2} \\ &\quad + 2\gamma^n (1 - \gamma^n) \frac{\rho_0}{d}, \end{aligned} \quad (20)$$

$$\text{Tr}(\rho^2[n]) = \gamma^{2n} + \frac{(1 - \gamma^n)^2}{d} + \frac{2\gamma^n(1 - \gamma^n)}{d}, \quad (21)$$

$$= \left(1 - \frac{1}{d}\right) \gamma^{2n} + \frac{1}{d}. \quad (22)$$

Therefore, we fit the data to  $A\gamma^{2n} + B$  and label the quantity  $\epsilon = \frac{3}{4}(1 - \gamma^{2/3})$  as the purity error (per the iSWAP gate). This procedure gives  $\epsilon = 2.2 \times 10^{-2}$ , comparable to our gate error, demonstrating that our gate is dominated by incoherent errors.

## V. DISCUSSION

In this paper, we demonstrate a high-fidelity universal two-qubit gate by parametric modulation of a tunable bus. The strength of the gate is not a strong function of the detuning between the qubits  $\Delta_{ij}$ . By contrast, drive-activated gates couple between manifolds, so the higher-level states are invariably coupled to the computational basis by the drive. As a result, the strength of the two-qubit terms decreases when  $\Delta_{ij}$  is larger than  $\alpha$  because, from the perspective of one qubit, the other qubit appears to be increasingly harmonic. For the device presented in this work,  $\Delta_{12, \delta=0}/2\pi = 854$  MHz, the leading drive-activated gate, cross-resonance, would not be viable [21]. As quantum circuits scale up, it is important to have qubits far apart in frequency to prevent addressability errors and cross talk. For example, calculations on the cross-resonance gate with several qubits coupled to the same bus indicate that there are a number of unwanted resonant detuning conditions between pairs which will be difficult to avoid with qubits spaced closer than  $\alpha$  [43,44].

There is room for improvement in the gate error we measured. Since the error is effectively coherence limited, we could decrease the gate time or increase the coherence. Decreasing the gate time may be difficult because of the leakage issues observed in simulation. Increasing the exchange coupling by increasing the qubit-bus coupling  $g$  may also be difficult; this process could also increase leakage and will certainly increase the parasitic ZZ interaction. Optimizing the gate time is an area for more consideration. Increasing coherence is less problematic and, for coherences

measured in comparable devices at IBM,  $T_1 = T_2 = 80 \mu\text{s}$  [45], gate errors should be  $< 5 \times 10^{-3}$  and also competitive with the best reported two-qubit gate errors  $9 \times 10^{-3}$  [12] and  $6 \times 10^{-3}$  [46].

As discussed in Sec. II A, there is no fundamental limit to the number of qubits that can be coupled via a tunable bus since the coupling occurs resonantly at the detuning between pairs. Understanding the role of noise, cross talk, and operability with multiple qubits coupled to the same tunable bus is, therefore, an important open question for this architecture. In particular, four qubits coupled through a single tunable bus could serve as a surface-code unit cell.

## ACKNOWLEDGMENTS

We acknowledge Firat Solgun, George Keefe, and Markus Brink for the simulation, layout, and fabrication of devices. We acknowledge the useful discussions with Sarah Sheldon, Lev Bishop, Jared Hertzberg, and Matthias Steffen. This work was supported by the Army Research Office under Contract No. W911NF-14-1-0124.

- 
- [1] Jay M. Gambetta, Jerry M. Chow, and Matthias Steffen, Building logical qubits in a superconducting quantum computing system, [arXiv:1510.04375](https://arxiv.org/abs/1510.04375).
  - [2] Austin G. Fowler, Matteo Mariantoni, John M. Martinis, and Andrew N. Cleland, Surface codes: Towards practical large-scale quantum computation, *Phys. Rev. A* **86**, 032324 (2012).
  - [3] L. DiCarlo, J. M. Chow, J. M. Gambetta, Lev S. Bishop, B. R. Johnson, D. I. Schuster, J. Majer, A. Blais, L. Frunzio, S. M. Girvin, and R. J. Schoelkopf, Demonstration of two-qubit algorithms with a superconducting quantum processor, *Nature (London)* **460**, 240 (2009).
  - [4] R. C. Bialczak, M. Ansmann, M. Hofheinz, E. Lucero, M. Neeley, A. D. O'Connell, D. Sank, H. Wang, J. Wenner, M. Steffen, A. N. Cleland, and J. M. Martinis, Quantum process tomography of a universal entangling gate implemented with Josephson phase qubits, *Nat. Phys.* **6**, 409 (2010).
  - [5] Jens Koch, Terri M. Yu, Jay Gambetta, A. A. Houck, D. I. Schuster, J. Majer, Alexandre Blais, M. H. Devoret, S. M. Girvin, and R. J. Schoelkopf, Charge-insensitive qubit design derived from the Cooper pair box, *Phys. Rev. A* **76**, 042319 (2007).
  - [6] Andrew J. Kerman and William D. Oliver, High-Fidelity Quantum Operations on Superconducting Qubits in the Presence of Noise, *Phys. Rev. Lett.* **101**, 070501 (2008).
  - [7] Ying-Dan Wang, A. Kemp, and K. Semba, Coupling superconducting flux qubits at optimal point via dynamic decoupling with the quantum bus, *Phys. Rev. B* **79**, 024502 (2009).
  - [8] Andrew J. Kerman, Quantum information processing using quasiclassical electromagnetic interactions between qubits and electrical resonators, *New J. Phys.* **15**, 123011 (2013).
  - [9] P.-M. Billangeon, J. S. Tsai, and Y. Nakamura, Scalable architecture for quantum information processing with

- superconducting flux qubits based on purely longitudinal interactions, *Phys. Rev. B* **92**, 020509(R) (2015).
- [10] Nicolas Didier, Jérôme Bourassa, and Alexandre Blais, Fast Quantum Nondemolition Readout by Parametric Modulation of Longitudinal Qubit-Oscillator Interaction, *Phys. Rev. Lett.* **115**, 203601 (2015).
- [11] Susanne Richer and David DiVincenzo, Circuit design implementing longitudinal coupling: A scalable scheme for superconducting qubits, *Phys. Rev. B* **93**, 134501 (2016).
- [12] Sarah Sheldon, Easwar Magesan, Jerry M. Chow, and Jay M. Gambetta, Procedure for systematically tuning up cross-talk in the cross-resonance gate, *Phys. Rev. A* **93**, 060302 (2016).
- [13] Hanhee Paik, D. I. Schuster, Lev S. Bishop, G. Kirchmair, G. Catelani, A. P. Sears, B. R. Johnson, M. J. Reagor, L. Frunzio, L. I. Glazman, S. M. Girvin, M. H. Devoret, and R. J. Schoelkopf, Observation of High Coherence in Josephson Junction Qubits Measured in a Three-Dimensional Circuit QED Architecture, *Phys. Rev. Lett.* **107**, 240501 (2011).
- [14] Chad Rigetti, Jay M. Gambetta, Stefano Poletto, B. L. T. Plourde, Jerry M. Chow, A. D. Córcoles, John A. Smolin, Seth T. Merkel, J. R. Rozen, George A. Keefe, Mary B. Rothwell, Mark B. Ketchen, and M. Steffen, Superconducting qubit in a waveguide cavity with a coherence time approaching 0.1 ms, *Phys. Rev. B* **86**, 100506 (2012).
- [15] Alexandre Blais, Jay Gambetta, A. Wallraff, D. I. Schuster, S. M. Girvin, M. H. Devoret, and R. J. Schoelkopf, Quantum-information processing with circuit quantum electrodynamics, *Phys. Rev. A* **75**, 032329 (2007).
- [16] P. J. Leek, S. Filipp, P. Maurer, M. Baur, R. Bianchetti, J. M. Fink, M. Göppl, L. Steffen, and A. Wallraff, Using sideband transitions for two-qubit operations in superconducting circuits, *Phys. Rev. B* **79**, 180511 (2009).
- [17] S. Poletto, Jay M. Gambetta, Seth T. Merkel, John A. Smolin, Jerry M. Chow, A. D. Córcoles, George A. Keefe, Mary B. Rothwell, J. R. Rozen, D. W. Abraham, Chad Rigetti, and M. Steffen, Entanglement of Two Superconducting Qubits in a Waveguide Cavity via Monochromatic Two-Photon Excitation, *Phys. Rev. Lett.* **109**, 240505 (2012).
- [18] Jerry M. Chow, Jay M. Gambetta, Andrew W. Cross, Seth T. Merkel, Chad Rigetti, and M. Steffen, Microwave-activated conditional-phase gate for superconducting qubits, *New J. Phys.* **15**, 115012 (2013).
- [19] Chad Rigetti, Alexandre Blais, and Michel Devoret, Protocol for Universal Gates in Optimally Biased Superconducting Qubits, *Phys. Rev. Lett.* **94**, 240502 (2005).
- [20] Chad Rigetti and Michel Devoret, Fully microwave-tunable universal gates in superconducting qubits with linear couplings and fixed transition frequencies, *Phys. Rev. B* **81**, 134507 (2010).
- [21] Jerry M. Chow, A. D. Córcoles, Jay M. Gambetta, Chad Rigetti, B. R. Johnson, John A. Smolin, J. R. Rozen, George A. Keefe, Mary B. Rothwell, Mark B. Ketchen, and M. Steffen, Simple All-Microwave Entangling Gate for Fixed-Frequency Superconducting Qubits, *Phys. Rev. Lett.* **107**, 080502 (2011).
- [22] P. Bertet, C. J. P. M. Harmans, and J. E. Mooij, Parametric coupling for superconducting qubits, *Phys. Rev. B* **73**, 064512 (2006).
- [23] S. H. W. van der Ploeg, A. Izmailkov, Alec Maassen van den Brink, U. Hübner, M. Grajcar, E. Il'ichev, H.-G. Meyer, and A. M. Zagoskin, Controllable Coupling of Superconducting Flux Qubits, *Phys. Rev. Lett.* **98**, 057004 (2007).
- [24] Yu Chen *et al.*, Qubit Architecture with High Coherence and Fast Tunable Coupling, *Phys. Rev. Lett.* **113**, 220502 (2014).
- [25] F. Wulschner *et al.*, Tunable coupling of transmission-line microwave resonators mediated by an rf squid, *EPJ Quant. Technol.* **3**, 10 (2016).
- [26] M. S. Allman, J. D. Whittaker, M. Castellanos-Beltran, K. Cicak, F. da Silva, M. P. DeFeo, F. Lecocq, A. Sirois, J. D. Teufel, J. Aumentado, and R. W. Simmonds, Tunable Resonant and Nonresonant Interactions between a Phase Qubit and *lc* Resonator, *Phys. Rev. Lett.* **112**, 123601 (2014).
- [27] Antti O. Niskanen, Yasunobu Nakamura, and Jaw-Shen Tsai, Tunable coupling scheme for flux qubits at the optimal point, *Phys. Rev. B* **73**, 094506 (2006).
- [28] M. Wallquist, V. S. Shumeiko, and G. Wendin, Selective coupling of superconducting charge qubits mediated by a tunable stripline cavity, *Phys. Rev. B* **74**, 224506 (2006).
- [29] K. Harrabi, F. Yoshihara, A. O. Niskanen, Y. Nakamura, and J. S. Tsai, Engineered selection rules for tunable coupling in a superconducting quantum circuit, *Phys. Rev. B* **79**, 020507 (2009).
- [30] H. Wang, Matteo Mariantoni, Radoslaw C. Bialczak, M. Lenander, Erik Lucero, M. Neeley, A. D. O'Connell, D. Sank, M. Weides, J. Wenner, T. Yamamoto, Y. Yin, J. Zhao, John M. Martinis, and A. N. Cleland, Deterministic Entanglement of Photons in Two Superconducting Microwave Resonators, *Phys. Rev. Lett.* **106**, 060401 (2011).
- [31] J. D. Whittaker, F. C. S. da Silva, M. S. Allman, F. Lecocq, K. Cicak, A. J. Sirois, J. D. Teufel, J. Aumentado, and R. W. Simmonds, Tunable-cavity QED with phase qubits, *Phys. Rev. B* **90**, 024513 (2014).
- [32] Christian Kraglund Andersen and Klaus Mølmer, Multi-frequency modes in superconducting resonators: Bridging frequency gaps in off-resonant couplings, *Phys. Rev. A* **91**, 023828 (2015).
- [33] S. J. Srinivasan, A. J. Hoffman, J. M. Gambetta, and A. A. Houck, Tunable Coupling in Circuit Quantum Electrodynamics Using a Superconducting Charge Qubit with a V-Shaped Energy Level Diagram, *Phys. Rev. Lett.* **106**, 083601 (2011).
- [34] Eva Zakka-Bajjani, François Nguyen, Minhya Lee, Leila R. Vale, Raymond W. Simmonds, and José Aumentado, Quantum superposition of a single microwave photon in two different "colour" states, *Nat. Phys.* **7**, 599 (2011).
- [35] Eliot Kapit, Universal two-qubit interactions, measurement, and cooling for quantum simulation and computing, *Phys. Rev. A* **92**, 012302 (2015).
- [36] J. Majer, J. M. Chow, J. M. Gambetta, Jens Koch, B. R. Johnson, J. A. Schreier, L. Frunzio, D. I. Schuster, A. A. Houck, A. Wallraff, A. Blais, M. H. Devoret, S. M. Girvin, and R. J. Schoelkopf, Coupling superconducting qubits via a cavity bus, *Nature (London)* **449**, 443 (2007).

- [37] A. Dewes, F. R. Ong, V. Schmitt, R. Lauro, N. Boulant, P. Bertet, D. Vion, and D. Esteve, Characterization of a Two-Transmon Processor with Individual Single-Shot Qubit Readout, *Phys. Rev. Lett.* **108**, 057002 (2012).
- [38] Joydip Ghosh and Austin G. Fowler, Leakage-resilient approach to fault-tolerant quantum computing with superconducting elements, *Phys. Rev. A* **91**, 020302 (2015).
- [39] See Supplemental Material at <http://link.aps.org/supplemental/10.1103/PhysRevApplied.6.064007> for the experimental setup and single qubit coherence data.
- [40] Easwar Magesan, J. M. Gambetta, and Joseph Emerson, Scalable and Robust Randomized Benchmarking of Quantum Processes, *Phys. Rev. Lett.* **106**, 180504 (2011).
- [41] Easwar Magesan, Jay M. Gambetta, B. R. Johnson, Colm A. Ryan, Jerry M. Chow, Seth T. Merkel, Marcus P. da Silva, George A. Keefe, Mary B. Rothwell, Thomas A. Ohki, Mark B. Ketchen, and M. Steffen, Efficient Measurement of Quantum Gate Error by Interleaved Randomized Benchmarking, *Phys. Rev. Lett.* **109**, 080505 (2012).
- [42] Joel Wallman, Chris Granade, Robin Harper, and Steven T Flammia, Estimating the coherence of noise, *New J. Phys.* **17**, 113020 (2015).
- [43] Easwar Magesan (private communication).
- [44] Maika Takita, A. D. Córcoles, Easwar Magesan, Baleegh Abdo, Markus Brink, Andrew Cross, Jerry M. Chow, and Jay M. Gambetta, Demonstration of Weight-Four Parity Measurements in the Surface Code Architecture, *Phys. Rev. Lett.* **117**, 210505 (2016).
- [45] IBM Quantum Experience, <http://www.ibm.com/quantumcomputing> (2016).
- [46] R. Barends *et al.*, Superconducting quantum circuits at the surface code threshold for fault tolerance, *Nature (London)* **508**, 500 (2014).